

## Accepted Manuscript

Saturn's auroral morphology and field-aligned currents during a solar wind compression

S.V. Badman, G. Provan, E.J. Bunce, D.G. Mitchell, H. Melin, S.W.H. Cowley, A. Radioti, W.S. Kurth, W.R. Pryor, J.D. Nichols, S.L. Jinks, T.S. Stallard, R.H. Brown, K.H. Baines, M.K. Dougherty

PII: S0019-1035(14)00642-3  
DOI: <http://dx.doi.org/10.1016/j.icarus.2014.11.014>  
Reference: YICAR 11366

To appear in: *Icarus*

Received Date: 9 June 2014  
Revised Date: 24 October 2014  
Accepted Date: 7 November 2014

Please cite this article as: Badman, S.V., Provan, G., Bunce, E.J., Mitchell, D.G., Melin, H., Cowley, S.W.H., Radioti, A., Kurth, W.S., Pryor, W.R., Nichols, J.D., Jinks, S.L., Stallard, T.S., Brown, R.H., Baines, K.H., Dougherty, M.K., Saturn's auroral morphology and field-aligned currents during a solar wind compression, *Icarus* (2014), doi: <http://dx.doi.org/10.1016/j.icarus.2014.11.014>

This is a PDF file of an unedited manuscript that has been accepted for publication. As a service to our customers we are providing this early version of the manuscript. The manuscript will undergo copyediting, typesetting, and review of the resulting proof before it is published in its final form. Please note that during the production process errors may be discovered which could affect the content, and all legal disclaimers that apply to the journal pertain.



1 Saturn's auroral morphology and field-aligned currents  
 2 during a solar wind compression

3 S. V. Badman<sup>a</sup>, G. Provan<sup>b</sup>, E. J. Bunce<sup>b</sup>, D. G. Mitchell<sup>c</sup>, H. Melin<sup>b,d</sup>,  
 4 S. W. H. Cowley<sup>b</sup>, A. Radioti<sup>e</sup>, W. S. Kurth<sup>f</sup>, W. R. Pryor<sup>g</sup>, J. D. Nichols<sup>b</sup>,  
 5 S. L. Jinks<sup>b</sup>, T. S. Stallard<sup>b</sup>, R. H. Brown<sup>h</sup>, K. H. Baines<sup>i</sup>, M. K. Dougherty<sup>j</sup>

6 <sup>a</sup>*Department of Physics, Lancaster University, Bailrigg, Lancaster, LA1 4YB, UK*

7 <sup>b</sup>*Department of Physics and Astronomy, University of Leicester, University Road,  
 8 Leicester, LE1 7RH, UK*

9 <sup>c</sup>*JHU APL, 111999 Johns Hopkins Road, Laurel, MD 20723, USA*

10 <sup>d</sup>*Space Environment Technologies, USA*

11 <sup>e</sup>*LPAP - Université de Liège, Sart Tilman - B5c, 17 Allé du 6 Aout, 4000 - LIEGE,  
 12 Belgium*

13 <sup>f</sup>*Department of Physics and Astronomy, University of Iowa, 613 Van Allen Hall, Iowa  
 14 City, IA 52242-1479, USA*

15 <sup>g</sup>*Central Arizona College, Coolidge, AZ 85128, USA*

16 <sup>h</sup>*LPL, University of Arizona, Tucson, AZ 85721, USA*

17 <sup>i</sup>*JPL, Pasadena, CA 91109, USA*

18 <sup>j</sup>*Imperial College London, London, SW7 2AZ, UK*

---

19 **Abstract**

On 21–22 April 2013, during a coordinated auroral observing campaign, instruments onboard Cassini and the Hubble Space Telescope observed Saturn's aurora while Cassini traversed Saturn's high latitude auroral field lines. Signatures of upward and downward field-aligned currents were detected in the nightside magnetosphere in the magnetic field and plasma measurements. The location of the upward current corresponded to the bright ultraviolet auroral arc seen in the auroral images, and the downward current region was located poleward of the upward current in an aurorally dark region. Within the polar cap magnetic field and plasma fluctuations were identified with periods of  $\sim 20$  and  $\sim 60$  min. The northern and southern auroral ovals

were observed to rock in latitude in phase with the respective northern and southern planetary period oscillations. A solar wind compression impacted Saturn's magnetosphere at the start of 22 April 2013, identified by an intensification and extension to lower frequencies of the Saturn kilometric radiation, with the following sequence of effects: (1) intensification of the auroral field-aligned currents; (2) appearance of a localised, intense bulge in the dawnside (04–06 LT) aurora while the midnight sector aurora remained fainter and narrow; (3) latitudinal broadening and poleward contraction of the nightside aurora, where the poleward motion in this sector is opposite to that expected from a model of the auroral oval's usual oscillation. These observations are interpreted as the response to tail reconnection events, initially involving Vasyliunas-type reconnection of closed mass-loaded magnetotail field lines, and then proceeding onto open lobe field lines, causing the contraction of the polar cap region on the night side.

20 *Keywords:* Saturn, magnetosphere, Aurorae

---

## 21 **1. Introduction**

22 Saturn's auroral intensity and morphology are known to respond strongly  
23 to the solar wind conditions that envelop the magnetosphere. The 'quiet' au-  
24 rora is typically composed of a 1–2° wide arc, more intense on the dawn side  
25 than the dusk, and located at 14–16° co-latitude in the southern dayside  
26 sector (Grodent et al., 2005; Badman et al., 2006; Lamy et al., 2009; Car-  
27 bary, 2012). The northern aurora is typically located 1–2° closer to the pole  
28 than that in the south because of the higher magnetic field strength in the

29 northern hemisphere (Dougherty et al., 2005; Nichols et al., 2009). However,  
30 the location and width of the aurora are highly variable, and sub-structure  
31 of the oval is commonly seen (Badman et al., 2006, 2014b; Grodent et al.,  
32 2011; Meredith et al., 2013). Large-scale auroral intensifications have been  
33 observed in response to the arrival of solar wind shocks ahead of high pres-  
34 sure regions (Prangé et al., 2004; Clarke et al., 2005, 2009; Crary et al., 2005;  
35 Nichols et al., 2014). These intensifications have been interpreted as the  
36 signatures of compression-induced magnetotail reconnection (Cowley et al.,  
37 2005; Bunce et al., 2005b). Latitudinal broadening of the main auroral emis-  
38 sions and smaller-scale features have been related to intensifications of the  
39 ring current and to more localised injections in the magnetosphere (Mitchell  
40 et al., 2009a; Radioti et al., 2013b; Lamy et al., 2013). Small spot and arc  
41 features at and poleward of the main arcs of emission have been identified as  
42 the signatures of reconnection in both the dayside and nightside magneto-  
43 sphere (Gérard et al., 2005; Radioti et al., 2011, 2013a, 2014; Badman et al.,  
44 2012a, 2013; Jackman et al., 2013; Meredith et al., 2013, 2014). Measure-  
45 ments of field-aligned currents associated with the main auroral emission by  
46 Cassini have shown that the upward current carried by downward auroral  
47 electrons is co-located with the polar cap boundary on the day side (Bunce  
48 et al., 2008a) and maps to the outer ring current or outer magnetosphere on  
49 the night side (Talboys et al., 2011).

50 Many features of Saturn’s magnetosphere demonstrate so-called ‘plane-  
51 tary period oscillations’ in their intensity and/or location, as reviewed, for  
52 example, by Carbary & Mitchell (2013). The planetary period perturba-  
53 tions in the magnetic field at high latitudes take the form of planet-centered

54 transverse rotating dipoles in each hemisphere (Provan et al., 2009). The  
55 near-equatorial field perturbations take the form of quasi-uniform rotating  
56 fields aligned with the effective dipoles in the equatorial plane, combined with  
57 north-south fields, resulting in arched loops (Andrews et al., 2010). The effec-  
58 tive dipoles rotate independently in the northern and southern hemispheres  
59 with periods close to 10.7 h. Field-aligned currents are associated with these  
60 magnetic field perturbations. The currents are directed across the pole at  
61 high-latitudes, i.e. field-aligned downward into the ionosphere on one side of  
62 the pole, field-aligned upward from the ionosphere on the other side of the  
63 pole, and partially closing in the equatorial plane of the outer magnetosphere.

64 The planetary period oscillations are also evident in both the location  
65 and intensity of Saturn's aurora. The centres of the auroral ovals have  
66 been observed to oscillate along an ellipse with a latitudinal amplitude of  
67  $1\text{--}2^\circ$  (Nichols et al., 2008, 2010b). Nichols et al. (2010b) suggested that the  
68 northern auroral oval would be offset in the direction of the northern effec-  
69 tive rotating dipole, and the southern oval offset in the direction opposite to  
70 the southern effective rotating dipole. However, more recent work has indi-  
71 cated that the maximum equatorward displacement of the southern auroral  
72 oval occurs  $90^\circ$  ahead in azimuth of the southern effective dipole direction,  
73 equivalent to 6 h later in LT (G. Hunt and S.W.H. Cowley, personal commu-  
74 nication, 2014). Applying this to the northern hemisphere suggests that the  
75 northern auroral oval should exhibit its maximum equatorward displacement  
76  $90^\circ$  behind the northern effective dipole direction, equivalent to 6 h earlier  
77 in LT. The northern and southern auroral ovals are then expected to rock  
78 around their central positions in phase with the rotation of the northern and

79 southern effective transverse dipoles. The intensity of the aurora in each  
80 hemisphere is also shown to be modulated at the respective period accord-  
81 ing to the rotation of the field-aligned currents associated with the effective  
82 transverse dipoles, although a local time asymmetry also remains, as men-  
83 tioned above (Sandel et al., 1982; Nichols et al., 2010a; Badman et al., 2012b;  
84 Lamy et al., 2013; Carbary, 2013).

85 Saturn's aurora are most commonly observed at ultraviolet and infrared  
86 wavelengths, corresponding to emission from H and H<sub>2</sub> in the UV and H<sub>3</sub><sup>+</sup> in  
87 the infrared. Badman et al. (2011) and Melin et al. (2011, 2014) have shown  
88 that the main auroral arcs are co-located at these wavelengths such that the  
89 UV and IR main emissions can be directly compared. However, there are  
90 differences at higher and lower latitudes reflecting the different response of  
91 these emitting species to auroral electron energy, thermospheric temperature,  
92 or emitting species lifetime (Tao et al., 2011; Badman et al., 2014a).

93 It is clear from the discussion above that Saturn's aurorae respond to  
94 both external (solar wind) and internal (planetary rotation) dynamics. In  
95 this study the in situ and remote signatures of auroral precipitation are  
96 analysed over an interval from the 2013 coordinated observing campaign.  
97 This interval included observations of both the northern and southern aurorae  
98 and the response to a solar wind compression. These observations provide an  
99 opportunity to disentangle the planetary period rocking of the auroral oval  
100 from a localised poleward contraction in response to solar wind compression-  
101 driven magnetotail dynamics. In the sections below we first describe the field  
102 and particle measurements made by Cassini and then show the sequence of  
103 auroral observations. These observations are then related to each other,

104 the rocking of the auroral oval identified, and the effects of the solar wind  
105 compression investigated.

## 106 **2. In situ observations of fields and particles by Cassini**

107 Figure 1 shows the observations made by Cassini on 2013-111 and 2013-  
108 112, around the periapsis of Rev 187 which occurred at the end of 2013-111.  
109 Cassini was moving from the southern pre-midnight sector to the northern  
110 post-midnight sector. The upper panel shows the electric field spectrogram  
111 detected by the Radio and Plasma Wave Science instrument (RPWS, Gurnett  
112 et al., 2004), with Saturn Kilometric Radiation (SKR) evident at 100s of kHz  
113 and broadband auroral hiss at up to  $\sim 100$  Hz. The magnetic field measured  
114 by the magnetometer (Dougherty et al., 2004) is plotted in spherical polar  
115 coordinates referenced to the planet's dipole axis (which is closely aligned  
116 with the spin axis) in the lower panel. The residual field components are  
117 plotted after subtraction of a model of the internal planetary magnetic field  
118 including dipole, quadrupole and octupole components (Burton et al., 2010).

119 At the start of the interval Cassini was traversing southern lobe field  
120 lines, indicated by the quiet magnetic field. The presence of auroral hiss  
121 in the electric field spectrogram in the upper panel is also associated with  
122 the high latitude magnetic field lines (Gurnett et al., 2010). The equatorial  
123 crossing from south to north is identified by the reversal of the  $B_r$  component  
124 of the field (green) from negative to positive.

125 Sharp changes in the azimuthal  $B_\phi$  component of the magnetic field were  
126 also observed. As discussed in several previous studies, localised perturba-  
127 tions in  $B_\phi$  are indicative of field-aligned currents, the upward portion of

128 which is associated with the auroral emission (Bunce et al., 2008a; Talboys  
 129 et al., 2009b,a, 2011; Badman et al., 2012a). The  $B_\phi$  component can be  
 130 used to derive the meridional ionospheric Pedersen current by application of  
 131 Ampère’s law to a current ring centered on the planet’s dipole axis. This  
 132 relationship is given by

$$I_P = \pm \frac{\rho B_\phi}{\mu_0}, \quad (1)$$

133

134 where  $I_P$  is the meridional ionospheric current per radian of azimuth,  $\rho$  is  
 135 the cylindrical radial distance of Cassini from Saturn’s dipole axis and the  
 136 negative sign applies for the northern hemisphere and positive for the south-  
 137 ern hemisphere (e.g. Bunce et al., 2008a; Talboys et al., 2011). This analysis  
 138 also assumes that the structures are stationary relative to the moving space-  
 139 craft, which is a reasonable assumption in this case as the spacecraft was at  
 140 small radial distance, 6–9  $R_S$ , and moving relatively quickly across the field  
 141 lines of interest. Assuming approximate axi-symmetry, increases and de-  
 142 creases in the meridional ionospheric current require downward and upward  
 143 field-aligned currents to maintain current continuity.

144 The  $B_\phi$  perturbations and deduced meridional ionospheric current are  
 145 shown for the intervals when Cassini crossed the southern and northern  
 146 nightside auroral current regions in Figure 2. Each of these shows a 12 h  
 147 sub-interval of that in Figure 1, with the southern encounter on 2013-111  
 148 (a–d) and the northern encounter on 2013-112 (e–h). Figures 2c and g show  
 149 the meridional ionospheric Pedersen current, positive equatorward, in black  
 150 (left hand axis). The ionospheric colatitude of the spacecraft is also shown in



151 grey (right hand axis) where the mapping to the ionosphere was performed  
 152 using the Burton et al. (2010) model of the planetary field plus a contribution  
 153 from the ring current modelled by Bunce et al. (2008b). Figures 2d and h  
 154 show the  $B_\phi$  perturbations from which  $I_P$  was derived.

155 The large scale structure of the field-aligned currents identified during  
 156 these intervals is as follows: the increase from  $B_\phi \sim 0$  to  $B_\phi > 0$  at 14 UT on  
 157 2013-111, as Cassini moved equatorward in the southern hemisphere, indi-  
 158 cates a field-aligned current directed downward into the southern ionosphere.  
 159 This was followed by the opposite signature indicating an upward current at  
 160 18 UT. These downward and upward currents are indicated by the orange  
 161 and purple shading, respectively, on Figure 2c. The magnitude of the upward  
 162 current was  $\sim 2.3 \text{ MA rad}^{-1}$ . In the northern hemisphere on 2013-112 the  
 163 strong reversal from  $B_\phi > 0$  to  $B_\phi < 0$  at 03:40 UT, while Cassini travelled  
 164 poleward, indicates an upward current of magnitude  $\sim 5.1 \text{ MA rad}^{-1}$ . This  
 165 is indicated by the purple shading on Figure 2f. The upward current was  
 166 followed by an overall decrease in the  $B_\phi$  magnitude until 07 UT, indicative  
 167 of downward current (orange shading on Figure 2f).

168 The signatures of the field-aligned currents in the plasma and wave ob-  
 169 servations are now examined. Figure 2a shows two notable spikes in the  
 170 broadband wave power at 12:30 UT and 13:30 UT on 2013-111, extending to  
 171  $\sim 1 \text{ kHz}$ . During these spikes the lower frequency, quasi-continuous emission  
 172 disappeared, which could be a signature of Cassini passing through the edge  
 173 of the resonance cone, where it can only detect the higher frequencies (Kopf,  
 174 2010). The second and more intense of the spikes followed a small, sharp  
 175 increase in  $B_\phi$  within the downward current region indicated by the orange

176 shading on Figure 2c, while the first spike was detected just outside the down-  
177 ward current region. The LEMMS sensor also detected an increased flux of  
178 electrons at energies of a few tens of keV during this interval from 2013-111  
179 12:20–14:10 UT, shown in Figure 2b. These observations suggest narrow or  
180 transient enhancements of the downward current structure detected between  
181 2013-111 13:00–14:40 UT (orange shading). This is consistent with the in-  
182 creased flux of energetic electrons - supposed to be travelling upward to the  
183 spacecraft. No similar spikes in the broadband wave power were observed  
184 during the upward current encounters indicated by the purple shading on  
185 Figures 2c and g at  $\sim 17:30$ – $18:00$  UT on 2013-111 and  $03:00$ – $04:30$  UT on  
186 2013-112. The broadband waves (up to  $\sim 100$  Hz) seen in Figures 2a and e  
187 were not detected in the regions equatorward of the upward current in either  
188 the northern or southern hemisphere, as shown by Gurnett et al. (2010).

189 During and after the encounter with the upward current region at  $03:00$ –  
190  $04:30$  UT on 2013-112 all components of the magnetic field exhibited repeated  
191 small fluctuations until  $\sim 12$  UT (see the lower panel of Figure 1 and Fig-  
192 ure 2h). Two spikes in the broadband waves (up to  $\sim 100$  Hz) were detected  
193 by RPWS at  $\sim 06$  and  $07$  UT (Figure 2e), similar to those observed at  $12:30$   
194 and  $13:30$  UT on 2013-111 (shown in Figure 2a). Small fluctuations in  $B_\phi$   
195 towards lower values also occurred at these times, within the downward cur-  
196 rent region indicated by the orange shading on Figure 2g. Figure 2f shows  
197 energetic proton fluxes measured by the Ion Neutral Camera (INCA), part  
198 of the Magnetospheric Imaging Instrument (MIMI, Krimigis et al., 2004).  
199 Peaks in the 90–360 keV proton fluxes were also detected at  $06$  and  $07$  UT  
200 on 2013-112. These wave and plasma intensifications are commonly seen in

201 Cassini observations and have been related to strong downward current re-  
202 gions, although the cause of the  $\sim 1$  h periodicity is unknown (Mitchell et al.,  
203 2009b, 2014; Badman et al., 2012a; Roussos et al., 2014).

204 From approximately 07–12 UT on 2013-112 the field fluctuations were  
205 of smaller magnitude (up to 1 nT) and more regular (Figure 2h). During  
206 this interval smaller peaks in the proton fluxes (Figure 2f) and broadband  
207 wave intensity (Figure 2e) were also present. The period of these smaller  
208 fluctuations was approximately 20 min. At this time Cassini was moving  
209 sunward across the northern polar cap at high latitudes within the auroral  
210 oval.

211 The electric field spectra shown in Figure 1 and 2e show that the SKR  
212 intensified and extended to lower frequencies from  $\sim 5$  UT on 2013-112. This  
213 is indicative of a solar wind compression of the magnetosphere (Kurth et al.,  
214 2005; Badman et al., 2008) and signifies an increased flux of field-aligned,  
215 accelerated electrons and an extension of the SKR source region to higher  
216 altitudes.

### 217 3. Auroral observations

218 Three instruments were used to make auroral observations during this  
219 interval. Infrared auroral emission from the molecular ion  $\text{H}_3^+$  was detected by  
220 the Cassini Visual and Infrared Mapping Spectrometer (VIMS, Brown et al.,  
221 2004). VIMS acquires a full wavelength spectrum (0.85–5.1  $\mu\text{m}$ ) at each pixel  
222 position in its field of view (FOV) sequentially, where 1 pixel =  $0.5 \times 0.5$  mrad  
223 and the maximum FOV is  $64 \times 64$  pixels. The total time required to build  
224 up a 2-D pseudo-image was 72 min for the observations used in this study.

225 The data were projected onto a  $0.25^\circ \times 0.25^\circ$  planetocentric polar grid using  
226 the peak emission height of 1100 km above the 1 bar reference spheroid  
227 (Stallard et al., 2012). The emission intensities used here were determined  
228 from multiple wavelength bins containing  $H_3^+$  emission lines around 3.5  $\mu\text{m}$ .

229 The UV aurorae were observed by the Cassini Ultraviolet Imaging Spec-  
230 trometer (UVIS, Esposito et al., 2004) and the Hubble Space Telescope  
231 (HST) Advanced Camera for Surveys (ACS). The UVIS observations were  
232 acquired by scanning the slit ( $1.5 \times 64$  mrad) across the auroral region, observ-  
233 ing the wavelength range 115.5–191.2 nm. Pseudo-images were constructed  
234 by combining three slit scans covering different portions of the auroral region  
235 using the method described by Grodent et al. (2011). Each pseudo-image  
236 composed of three scans took about 80 min to build up. These images were  
237 polar projected onto a  $0.1^\circ \times 0.1^\circ$  planetocentric polar grid using the peak  
238 emission height for  $H_2$  emission of 1100 km above the 1 bar reference spheroid  
239 (Gérard et al., 2009).

240 Turning to the HST observations, the Solar Blind Channel (SBC) of ACS  
241 has a FOV of  $35 \times 31$  arcsec<sup>2</sup> and an average plate scale of  $\sim 0.032$  arc-  
242 sec pixel<sup>-1</sup>. The image processing pipeline is described in detail by Clarke  
243 et al. (2009). The images used in this study were taken using the F115LP  
244 long-pass filter which includes emission from H Lyman- $\alpha$  and  $H_2$  Lyman and  
245 Werner bands in the range 115–170 nm. The exposure time was 15 min for  
246 each image. These were also polar projected onto a  $0.1^\circ \times 0.1^\circ$  planetocentric  
247 polar grid using the peak emission height of 1100 km above the 1 bar refer-  
248 ence spheroid. Note that as each instrument covers a different wavelength  
249 range we do not compare intensities in this study but instead interpret the

250 shape and location of the emission in each case.

251 The sequence of observations of Saturn's aurora during this interval is  
252 shown in Figures 3 and 4. Figure 3a is a pseudo-image of the southern  
253 infrared aurora taken by Cassini VIMS, where the view is looking down  
254 through the planet to the southern pole with dawn to the left and dusk to the  
255 right. The remaining images are of the northern aurora taken by HST/ACS  
256 (3b, 3c, and 4d), UVIS (4a and b) and VIMS (4c), looking down on the  
257 northern pole with local noon at the bottom, dawn to the left and dusk to  
258 the right. The yellow grid indicates latitudes at  $10^\circ$  intervals. The white line  
259 indicates the trajectory of Cassini mapped to the appropriate hemisphere  
260 using the Burton et al. (2010) model of Saturn's magnetic field and a model  
261 ring current from Bunce et al. (2008b). The white labelled circles indicate the  
262 start of days 111–113, and the yellow square indicates the magnetic footprint  
263 of Cassini along this path at the central time of the image in each panel (the  
264 times labelled in the upper right corner of each panel). The orange and  
265 purple shaded portions of the trajectory indicate the regions of downward  
266 and upward field aligned current, respectively, identified from the magnetic  
267 field data. For the images taken on 2013-111 and shown in Figure 3 these are  
268 the southern hemisphere current regions identified on 2013-111 in Figure 2c.  
269 For the images taken on 2013-112 and shown in Figure 4 they are the northern  
270 hemisphere current regions identified on 2013-112 in Figure 2g. The dashed  
271 yellow arrow shows the direction in which the auroral oval is expected to be  
272 tilted at that time, where in the southern hemisphere (Figure 3a), this is  $90^\circ$   
273 ahead in azimuth of the southern effective rotating transverse dipole, and  
274 in the northern hemisphere it is  $90^\circ$  behind the northern effective rotating

275 transverse dipole (G. Hunt and S.W.H. Cowley, personal communication,  
276 2014). The azimuthal directions of the effective dipoles are taken from the  
277 empirical model by Provan et al. (2014).

278 The VIMS observations in Figure 3a at 09:14 UT on 2013-111 show a  
279 very narrow auroral arc,  $< 1^\circ$  latitude wide, with a discontinuity at local  
280 midnight. The intense patches at the pre-midnight edge of the instrument  
281 field of view are contamination from scattered light and do not represent  
282 auroral emission. The discontinuity in the auroral arc was observed to rotate  
283 to later LT over the three VIMS images taken on this day (of which the first  
284 is shown here) and may be related to a flow discontinuity or superposition of  
285 the rotating field-aligned currents. The sequence of VIMS observations and  
286 the possible causes of the discontinuity are described in more detail by Melin  
287 et al. (2014). A few hours later HST observed the northern UV aurora, shown  
288 in Figures 3b and c. Although the midnight region conjugate to that observed  
289 in the south by VIMS was not visible because of the viewing geometry, the  
290 aurorae at other local times remained narrow, especially around dawn.

291 Figure 4a and b show observations of the northern ultraviolet aurorae  
292 made by Cassini UVIS during scans centered on 2013-112 03:32 and 05:06 UT.  
293 In the first of these observations the aurorae formed a relatively narrow arc  
294 ( $1\text{--}2^\circ$  latitude) of variable intensity extending from pre-midnight through  
295 dawn to pre-noon. In the second observation the arc had moved to slightly  
296 higher latitude and contained an intense bulge at 04–06 LT extending  $\sim 1^\circ$   
297 poleward of the centre of the arc.

298 Figure 4c shows two consecutive observations of the northern infrared  
299 aurora made by Cassini VIMS, centred on times of 2013-112 06:27 UT and

300 07:41 UT. The auroral arcs remained narrow and of variable intensity along  
301 the midnight region but became relatively wider ( $\sim 3^\circ$  latitude) and more  
302 intense in the pre-dawn region captured in the later image at 2013-112  
303 07:41 UT. (The patch of intense emission in the bottom left corner of the  
304 FOV at 2013-112 07:41 UT is again non-auroral contamination present at all  
305 wavelengths, while the arc identified at higher latitudes is auroral emission.)  
306 It is difficult to conclude whether the different auroral forms observed in  
307 these two images are caused by spatial or temporal variations. However, the  
308 previous UVIS image (Figure 4b) shows a similar morphology of a narrow  
309 midnight region and a broader pre-dawn region, such that it seems likely that  
310 the variations are spatial rather than just temporal.

311 Finally, Figure 4d shows an HST observation of the northern UV aurora  
312 at 2013-112 08:45 UT. The midnight region was not observed because of the  
313 viewing angle, but the post-midnight auroral arc was at higher latitude and  
314 broader ( $\sim 4^\circ$  latitude) than in previous observations. The most intense  
315 region was post-dawn.

#### 316 4. Correspondence between in situ and auroral observations

317 Comparison of Cassini's mapped trajectory and the southern auroral im-  
318 age shown in Figure 3a with the corresponding electric field spectra and mag-  
319 netic field measurements shown in Figure 2a-d shows that the spacecraft was  
320 on polar cap field lines poleward of the auroral oval (observed in the infrared)  
321 until after 12 UT on 2013-111. The downward current signature was iden-  
322 tified in the MAG data at 2013-111 14 UT while Cassini was on field lines  
323 mapping to  $15^\circ$  co-latitude in the southern ionosphere or  $\sim 14^\circ$  co-latitude

324 in the northern ionosphere. Figure 3c shows an image of the northern au-  
325 rora at the start of Cassini's encounter with the downward current region at  
326 13:36 UT on 2013-111. The sub-spacecraft portion of the aurora was not vis-  
327 ible at this time, but extrapolation between the pre- and post-midnight arcs  
328 of the aurora that were observed suggests that the downward current region  
329 was located just poleward of the nightside auroral arc. The upward current  
330 was encountered four hours later, when Cassini's position mapped to  $19^\circ$  in  
331 the southern hemisphere or  $17^\circ$  in the northern hemisphere. This suggests  
332 that the auroral current system and main emission had moved a few degrees  
333 equatorward in the time between the last auroral image (Figure 3c) and the  
334 in situ detection of the upward current, since it is the downward electrons  
335 carrying the upward current that are expected to generate the main auroral  
336 arc.

337 The next feature of interest is the strong upward field-aligned current  
338 detected by Cassini at 2013-112 03:40 UT as it moved to higher latitudes  
339 over the northern nightside region. This was detected during the UVIS scan  
340 interval used to build image Figure 4a. At this location the field line mapped  
341 to  $\sim 17^\circ$  co-latitude in the northern hemisphere as indicated on Figure 4a,  
342 which is at the poleward edge of the observed auroral arc. The full duration  
343 of the encounter with the upward current signature was 03:05–04:25 UT on  
344 2013-112, during which time Cassini moved  $1.5^\circ$  poleward in the ionosphere.  
345 This corresponds to the width of the auroral arc observed by UVIS:  $\sim 1^\circ$   
346 in this region, combined with the  $\sim 1^\circ$  poleward motion of the aurora arc  
347 which occurred between the two scans of this region shown in Figures 4a and  
348 b, therefore confirming the relationship, previously identified on the night



349 side by Bunce et al. (2014), between the upward current signature and the  
350 aurora.

351 As described in Section 2 above, the subsequent interval from 04–12 UT  
352 on 2013-112 was characterised by perturbations in the magnetic field, wave  
353 electric field, and proton fluxes and encompasses the region identified as a  
354 downward field-aligned current by the orange shading on Figure 2g. Through-  
355 out this interval Cassini was poleward of the aurora and moving sunward  
356 across the dark northern polar cap towards higher latitudes, as shown in  
357 Figures 4b–d. At 12 UT on 2013-112 Cassini reached a location of 06 LT, 9°  
358 colatitude, and 7.6  $R_S$  radial distance, from which point the signatures were  
359 no longer obvious in the magnetic field data and the measured auroral hiss  
360 became less intense. It is yet to be determined whether this decrease in the  
361 observed signals is due to rotation of the downward current region associated  
362 with the auroral hiss out of the range of detection by the spacecraft, or a  
363 change in spacecraft LT, latitude, or altitude. The cause of the periodicity  
364 in the downward current region is as yet unknown, and these observations  
365 show that, while the previously-known 1 h periodicity is detected for short  
366 intervals or restricted spatial regions in the southern and northern polar caps  
367 poleward of the upward current at the polar cap boundary, bursts occurring  
368 with a shorter period of approximately 20 mins are also detected at higher  
369 latitudes. These shorter period bursts were detected for long intervals, across  
370 a large spatial region and from a range of spacecraft altitudes. Their origin  
371 is being explored in an ongoing study.

## 372 5. Oscillation and contraction of the auroral oval

373 The locations of Saturn's auroral ovals have been observed to oscillate by  
374  $1\text{--}2^\circ$  in latitude in phase with the planetary period magnetic field pertur-  
375 bations (Nichols et al., 2008, 2010b). As described in the Introduction, the  
376 azimuth along which the centre of the northern oval is expected to be offset  
377 lags the azimuth of the northern effective transverse rotating dipole by  $90^\circ$ ,  
378 while the azimuth along which the centre of the southern oval is expected to  
379 be offset leads the azimuth of the southern effective dipole by  $90^\circ$ . The effec-  
380 tive dipoles rotate at the respective northern and southern rotation periods,  
381 such that the auroral ovals rock about their central position over the same  
382 periods.

383 The oscillations of the auroral oval are evident in the sequence of two  
384 HST images of the northern UV aurorae taken on 2013-111. In Figure 3b  
385 and c, the direction in which the oval is expected to be tilted is indicated by  
386 the yellow dashed arrow at the central time of each image. These arrows are  
387 reproduced in Figure 5, colour-coded according to the time of the image, as  
388 labelled in the top left corner. The location of the peak auroral emission on  
389 each image is also shown by the solid coloured lines. A circle was fitted to  
390 these points for each image and the circle centres are marked by the coloured  
391 crosses. The difference in azimuth of the northern effective dipole direction  
392 between these two images was  $\sim 50^\circ$  and the expected tilt of the auroral oval  
393 and its centre changes from being directed towards 18 LT to about 21:30 LT.  
394 The lines showing the location of the peak auroral emission at both dawn and  
395 dusk, and the crosses marking the fitted circle centres follow this predicted  
396 motion: tilting away from dusk at the time of the second image. The radii

397 of the fitted circles remained similar at  $15.2^\circ$  and  $14.8^\circ$  for the two images,  
398 confirming that this is a tilting of the oval, not an expansion.

399 The description in Section 4 of the correspondence between the field  
400 aligned currents and the auroral emission on 2013-111 also revealed that  
401 the upward field-aligned current was detected in the southern hemisphere  
402 mapping to a location  $\sim 1 - 2^\circ$  equatorward of where the southern nightside  
403 aurora was observed 4 h earlier (Figure 3a). At the time that the upward  
404 current was detected, 18 UT on 2013-111, the southern auroral oval was ex-  
405 pected to be tilted towards midnight, such that it would appear at its lowest  
406 latitudes in this sector. This is consistent with the detection of the upward  
407 current at lower latitudes than where the aurora were observed earlier in  
408 the day, and provides further evidence for the regular rocking of both the  
409 southern and northern auroral ovals on 2013-111.

410 The same analysis has been applied to the UVIS, VIMS, and HST images  
411 acquired on 2013-112 (Figures 4a–d), with results shown in Figure 6, covering  
412 approximately half a planetary period oscillation. The northern auroral oval  
413 was expected to be tilted towards dawn during the first image, then shift  
414 towards noon and finally duskward. The auroral oval was predicted to be  
415 most tilted towards noon during the image at 2013-112 06:27 UT (green  
416 line) such that the nightside part of the auroral oval should be located at  
417 its highest latitudes at this time. The cyan, yellow, and red lines showing  
418 the peak intensity of the observed aurorae in the later images were displaced  
419 duskward of that in the first image, as expected. The auroral emissions shown  
420 in Figures 4c and d cannot be fitted by a circle because of the limited FOV  
421 of the VIMS observations, and the poleward broadening of the aurora in the

422 post midnight region and poleward shift of the pre-noon arc in the final HST  
423 image. Therefore fitted circle centres are not shown for these images.

424 At the time of the last image, the northern auroral oval was expected to be  
425 displaced duskward and anti-sunward compared to the previous two images  
426 (green and yellow lines). The red line on Figure 6 shows that the oval had  
427 indeed shifted duskward compared to the earlier images (blue, cyan, yellow  
428 lines), however, the region closest to midnight had moved to higher latitudes  
429 instead of lower latitudes. Figure 4d shows that this contraction to higher  
430 latitudes is due to a combination of poleward broadening and motion of the  
431 post-midnight aurora as mentioned above. It is also apparent that the UV  
432 aurorae observed at 08:45 UT (Figure 4d) were generally thicker in latitude  
433 at most dawnside LT than in previous images. These observations clearly  
434 demonstrate that the change in location of the auroral oval during the latter  
435 part of the imaging interval was partly caused by a poleward contraction of  
436 the nightside aurorae, rather than purely the rocking of the auroral oval.

## 437 **6. Significance of solar wind compression**

438 Compression of the magnetosphere by the solar wind was inferred from  
439 the intensification and low frequency extension of the SKR emission early on  
440 2013-112. The sequence of auroral observations taken on this day suggests  
441 that the aurora moved poleward by as much as  $\sim 5^\circ$  latitude in the pre-  
442 dawn sector, over the 6 h between images Figure 4a and d. Only  $1\text{--}2^\circ$  of  
443 this motion is expected to be related to the regular oscillation of the oval.  
444 Furthermore the poleward contraction in the northern post-midnight region  
445 between the images at 06:27 and 08:45 UT on 2013-112 is opposite to the

446 tilting of the auroral oval expected here. These observations therefore reveal  
447 a contraction of the auroral oval in this sector. Sections of the dawnside oval  
448 were also observed to broaden in latitude and brighten relative to noon and  
449 midnight sections, which indicates increased electron precipitation in these  
450 regions.

451 In previous studies, solar wind compressions have been linked to broad  
452 and intense auroral displays across the dawnside polar region (Prangé et al.,  
453 2004; Clarke et al., 2005; Nichols et al., 2014), and exceptionally high latitude  
454 encounters with auroral field-aligned currents (Bunce et al., 2010). Features  
455 within and at the equatorward boundary of the main emission have also  
456 been related to the injection of plasma and dipolarisation of magnetic field  
457 in the magnetotail (Bunce et al., 2005b; Mitchell et al., 2009a; Jackman et al.,  
458 2013).

459 In the sequence of observations analysed here, a localised poleward bulge  
460 of the auroral emission was first observed in the pre-dawn region after 04:20  
461 on 2013-112, and then appeared to move sunward (Figures 4b and c). At this  
462 time the midnight arcs remained narrow. This was followed by a poleward  
463 broadening of the post-midnight aurora and contraction of the polar cap in  
464 this nightside region (Figure 4d). The SKR was intense throughout these  
465 observations and a low frequency extension was detected around 06 UT on  
466 2013-112 (Figure 2e).

467 The nightside upward and downward field-aligned currents were detected  
468 by Cassini in both hemispheres. The different duration of the field-aligned  
469 current encounters can be attributed to the relative motion of Cassini and the  
470 tilting auroral oval as described by Bunce et al. (2014). The upward current

471 encounter in the southern hemisphere at  $\sim 18$  UT on 2013-111 was short as  
472 Cassini moved equatorward while this section of the southern auroral oval  
473 moved poleward as the oval tilted towards noon (see Figures 2c and 5). The  
474 northern hemisphere upward current encounter lasted longer because Cassini  
475 was moving poleward while this region of the northern auroral oval was also  
476 moving poleward - as the oval again tilted towards noon (see Figures 2g and  
477 6).

478 The in situ measurements of the field-aligned currents show that the  
479 upward current measured in the northern hemisphere,  $5.1 \text{ MA rad}^{-1}$ , was  
480 more than twice as strong as that in the southern hemisphere on the previous  
481 day,  $2.3 \text{ MA rad}^{-1}$ . On average the nightside field-aligned currents have  
482 been shown to be of equal magnitude in both hemispheres (Talboys et al.,  
483 2011). Therefore we attribute the strengthening of the current measured in  
484 the northern hemisphere on 2013-112 to dynamics associated with the solar  
485 wind compression. Specifically, increased field-aligned current and electron  
486 precipitation in this region have been predicted and observed as a result of  
487 tail reconnection, which sets up a pair of upward and downward field-aligned  
488 currents linking the ionosphere with the newly-dipolarised magnetic field in  
489 the magnetotail (Cowley et al., 2005; Bunce et al., 2010; Jackman et al.,  
490 2013; Nichols et al., 2014).

491 The observations are consistent with an interval of tail reconnection oc-  
492 ccurring for several hours. The bulge in the pre-dawn auroral oval was ob-  
493 served during the second UVIS observing interval (Figure 4b), indicating  
494 that it appeared after 04:20 UT. As noted above, the magnitude of the up-  
495 ward field-aligned current and the SKR emission associated with the upward

496 current (downward auroral electrons) were enhanced at this time (Figure 2e  
497 and g). Jackman et al. (2009) have related the occurrence of enhanced and  
498 low frequency SKR to reconnection events occurring in Saturn's magnetotail.  
499 The auroral bulge was observed within the main emission on the dawn sec-  
500 tor, a region which maps to the outer ring current or outer magnetosphere  
501 (Belenkaya et al., 2014). The bulge is consistent with the injection of hot  
502 plasma into the dawnside outer magnetosphere following tail reconnection.  
503 However, other causes for the variability in the main oval structure have  
504 not been ruled out (Radioti et al., in preparation). Only the trailing edge  
505 of the bulge was visible in the next observation of this region at 07:41 UT  
506 (Figure 4c).

507 When the next VIMS image of the midnight region was taken, at 2013-  
508 112 06:27 UT, the location of the peak emission, shown in Figure 6, had  
509 shifted slightly poleward, but the image itself (Figure 4c) shows that a second,  
510 fainter but more continuous arc was still present at  $17^\circ$  co-latitude - the same  
511 as in the previous UVIS observation (Figure 4b). It is therefore not clear  
512 whether a poleward shift of the emission at midnight occurred between these  
513 observations. However, by the time of the final image, the shape of the aurora  
514 and the location of the peak emission shown in Figures 4d and 6 strongly  
515 suggest a poleward contraction of the oval in the post-midnight region. This  
516 is a signature of the closure of open magnetic flux from the magnetotail lobes  
517 (Cowley et al., 2005; Badman et al., 2005, 2014b; Nichols et al., 2014).

518 Compression of the magnetosphere by a high pressure region of the solar  
519 wind has been postulated to initiate reconnection in Saturn's magnetotail,  
520 as has been observed at the Earth (Boudouridis et al., 2003; Cowley et al.,

521 2005). In this scenario, reconnection begins on the radially-stretched, mass-  
522 loaded, closed field lines which contain the tail current sheet. This leads to  
523 the disconnection of a plasmoid and dipolarisation of the planetward mag-  
524 netic field lines - the tail part of the Vasyliunas cycle. These two effects  
525 (loss of mass via the disconnected plasmoid and planetward contraction of  
526 the connected field lines) then allow reconnection to proceed onto lobe field  
527 lines, closing open magnetic flux in the lobes as part of the Dungey cycle.  
528 The distinction and relationship between these processes has been described  
529 theoretically (e.g. Cowley et al., 2005), and detected in simulations (e.g. Jia  
530 et al., 2012) and observations (e.g. Jackman et al., 2011; Thomsen, 2013;  
531 Nichols et al., 2014).

532 We apply this sequence of events to describe the observations made dur-  
533 ing the current interval of study. On 2013-111 the aurorae were narrow,  
534 particularly on the night side, and demonstrated the regular planetary pe-  
535 riod rocking of the oval location (Figure 3). Early on 2013-112 a compression  
536 of the magnetosphere occurred, initially causing reconnection of closed, mass-  
537 loaded field lines in the central magnetotail. Plasma was injected into the  
538 outer ring current as the newly reconnected field lines contracted towards  
539 the planet and enhanced precipitation from this region resulted in intensi-  
540 fied SKR (Figure 2e) and a bulge in the pre-dawn auroral oval (Figure 4b),  
541 visible at 05 UT. At this time and over the next couple of hours, the au-  
542 roral oval near midnight remained narrow (Figure 4c). Reconnection then  
543 proceeded onto the open magnetotail lobe field lines, resulting in contraction  
544 of newly-closed field lines towards the planet. Field-aligned currents were  
545 set up in this region associated with the equatorward flow of the plasma at



546 the ionospheric footprint of these field lines, across the open-closed field line  
547 boundary. At 08:45 UT the auroral signature of this process was detected as  
548 the post-midnight auroral arc became relatively more intense, broadened in  
549 latitude, and contracted towards the pole (Figure 4d).

550 Finally we note that dayside magnetic reconnection is also expected to  
551 be stronger under solar wind compression conditions (Jackman et al., 2004;  
552 Badman et al., 2005, 2013), and would occur in the noon sector. A possible  
553 auroral signature of dayside reconnection may be identified in the HST image  
554 taken at the end of the observing interval (Figure 4d). The intensification  
555 and poleward shift of the aurora in this sector are consistent with emission  
556 expected in the vicinity of the open-closed field line boundary during day-  
557 side reconnection, although it is not certain whether this is a signature of  
558 low latitude reconnection resulting in the opening of magnetic flux, or re-  
559 connection with lobe field lines which would not change the amount of open  
560 flux (Bunce et al., 2005a; Gérard et al., 2005; Meredith et al., 2014). The  
561 lack of this feature earlier in the observing sequence illustrates that the tail  
562 reconnection and enhanced nightside currents are not triggered by recon-  
563 necting at the dayside magnetopause, as has been observed in the terrestrial  
564 magnetosphere (e.g. Anderson et al., 2014). Instead, tail reconnection can  
565 occur independently, although both processes are expected to be enhanced  
566 in solar wind compression regions.

## 567 7. Summary

568 We have examined the in situ and remote observations of Saturn's aurora  
569 in both the northern and southern hemispheres over a two-day interval during

570 the 2013 coordinated auroral campaign. Signatures of auroral field-aligned  
571 currents were identified in the magnetic field. The downward current regions  
572 were also identified by characteristic ion and auroral hiss intensifications.

573 On 2013-111 the auroral arcs observed in both hemispheres were narrow  
574 and the auroral ovals rocked in latitude in phase with the planetary period  
575 oscillations. Early on 2013-112 a solar wind compression arrived, as identified  
576 by an intensification and extension to lower frequencies of the SKR. At this  
577 time a bulge appeared along the pre-dawn auroral oval, which appeared to  
578 have moved sunward when this region was next observed. The midnight  
579 sector aurora remained a narrow arc at this time. Subsequently, the post-  
580 midnight aurora broadened in latitude and contracted towards the pole. The  
581 motion in this sector was in the opposite direction to that expected from the  
582 planetary period oscillation.

583 In the interval when the auroral imaging and current measurement were  
584 simultaneous in the northern hemisphere, the upward current corresponded  
585 to the bright nightside auroral arc and the downward current mapped to  
586 the aurorally dark region poleward of this. The upward field-aligned current  
587 associated with the northern main oval was more than twice as strong as  
588 its southern hemisphere counterpart measured on the previous day (5.1 MA  
589  $\text{rad}^{-1}$  compared to 2.3 MA  $\text{rad}^{-1}$ ).

590 These observations are interpreted as the auroral response to tail recon-  
591 nection instigated by solar wind compression of the magnetotail. The SKR  
592 intensification and auroral bulge are attributed to the injection of plasma  
593 into the outer ring current by reconnection on closed, mass-loaded tail field  
594 lines. The contraction of the reconnected field lines towards the planet then

595 allowed reconnection to proceed onto lobe field lines, closing the open flux,  
596 and resulting in a contraction of the auroral oval in the post-midnight sector.

597

598 **Acknowledgments** This work uses observations with the NASA/ESA Hub-  
599 ble Space Telescope obtained at the Space Telescope Science Institute (STScI),  
600 which is operated by AURA, inc. for NASA. SVB was supported by a Royal  
601 Astronomical Society Research Fellowship. EJB, GP, HM, SWHC and TSS  
602 were supported by STFC grant ST/K001000/1, and EJB by a Philip Lever-  
603 hulme Award. SLJ was supported by an STFC PhD studentship and JDN  
604 by an STFC Advanced Fellowship (ST/1004084/1). DGM was supported by  
605 the NASA Office of Space Science under Task Order 003 of contract NAS5-  
606 97271 between NASA Goddard Space flight Center and the Johns Hopkins  
607 University. The research at the University of Iowa was supported by NASA  
608 through contract 1415150 with the Jet Propulsion Laboratory.

## 609 **References**

610 Anderson, B. J., Korth, H., Waters, C. L., Green, D. L., Merkin, V. G.,  
611 Barnes, R. J., & Dyrud, L. P. (2014). Development of large-scale Birke-  
612 land currents determined from the Active Magnetosphere and Plane-  
613 tary Electrodynamics Response Experiment. *Geophys. Res. Lett.*, *41*.  
614 doi:10.1002/2014GL059941.

615 Andrews, D. J., Coates, A. J., Cowley, S. W. H., Dougherty, M. K., Lamy,  
616 L., Provan, G., & Zarka, P. (2010). Magnetospheric period oscillations  
617 at Saturn: Comparison of equatorial and high-latitude magnetic field pe-

618 riods with north and south Saturn kilometric radiation periods. *J. Geo-*  
619 *phys. Res.*, *115*, 12252. doi:10.1029/2010JA015666.

620 Badman, S. V., Achilleos, N., Arridge, C. S., Baines, K. H., Brown, R. H.,  
621 Bunce, E. J., Coates, A. J., Cowley, S. W. H., Dougherty, M. K., Fujimoto,  
622 M., Hospodarsky, G., Kasahara, S., Kimura, T., Melin, H., Mitchell, D. G.,  
623 Stallard, T., & Tao, C. (2012a). Cassini observations of ion and electron  
624 beams at Saturn and their relationship to infrared auroral arcs. *J. Geo-*  
625 *phys. Res.*, *117*. doi:10.1029/2011JA017222.

626 Badman, S. V., Achilleos, N., Baines, K. H., Brown, R. H., Bunce, E. J.,  
627 Dougherty, M. K., Melin, H., Nichols, J. D., & Stallard, T. (2011). Loca-  
628 tion of Saturn's northern infrared aurora determined from Cassini VIMS  
629 images. *Geophys. Res. Lett.*, *38*. doi:10.1029/2010GL046193.

630 Badman, S. V., Andrews, D. J., Cowley, S. W. H., Lamy, L., Provan, G.,  
631 Tao, C., Kasahara, S., Kimura, T., Fujimoto, M., Melin, H., Stallard,  
632 T., Brown, R. H., & Baines, K. H. (2012b). Rotational modulation and  
633 local time dependence of Saturn's infrared  $H_3^+$  auroral intensity. *J. Geo-*  
634 *phys. Res.*, *117*, A09228.

635 Badman, S. V., Branduardi-Raymont, G., Galand, M., Hess, S. L. G., Krupp,  
636 N., Lamy, L., Melin, H., & Tao, C. (2014a). Auroral Processes at the  
637 Giant Planets: Energy Deposition, Emission Mechanisms, Morphology and  
638 Spectra. *Space Sci. Rev.*, *180*. doi:10.1007/s11214-014-0042-x.

639 Badman, S. V., Bunce, E. J., Clarke, J. T., Cowley, S. W. H., Gérard, J.-C.,  
640 Grodent, D., & Milan, S. E. (2005). Open flux estimates in Saturn's magne-

- 641     tosphere during the January 2004 Cassini-HST campaign, and implications  
642     for reconnection rates. *J. Geophys. Res.*, *110*. doi:10.1029/2005JA011240.
- 643     Badman, S. V., Cowley, S. W. H., Gérard, J.-C., & Grodent, D. (2006). A  
644     statistical analysis of the location and width of Saturn's southern auroras.  
645     *Ann. Geophys.*, *24*, 3533–3545.
- 646     Badman, S. V., Cowley, S. W. H., Lamy, L., Cecconi, B., & Zarka, P. (2008).  
647     Relationship between solar wind corotating interaction regions and the  
648     phasing and intensity of Saturn kilometric radiation bursts. *Ann. Geophys.*,  
649     *26*, 3641–3651.
- 650     Badman, S. V., Jackman, C. M., Nichols, J. D., & Gérard, J.-C.  
651     (2014b). Open flux in Saturn's magnetosphere. *Icarus*, *231*, 137–145.  
652     doi:10.1016/j.icarus.2013.12.004.
- 653     Badman, S. V., Masters, A., Hasegawa, H., Fujimoto, M., Radioti, A., Gro-  
654     dent, D., Sergis, N., Dougherty, M. K., & Coates, A. J. (2013). Bursty  
655     magnetic reconnection at Saturn's magnetopause. *Geophys. Res. Lett.*, *40*,  
656     1027–1031. doi:10.1002/grl.50199.
- 657     Belenkaya, E. S., Cowley, S. W. H., Meredith, C. J., Nichols, J. D., Kalegaev,  
658     V. V., Alexeev, I. I., Barinov, O. G., Barinova, W. O., & Blokhina, M. S.  
659     (2014). Magnetospheric magnetic field modelling for the 2011 and 2012  
660     HST Saturn aurora campaigns - implications for auroral source regions.  
661     *Ann. Geophys.*, *32*, 689–704.

- 662 Boudouridis, A., Zesta, E., Lyons, R., Anderson, P. C., & Lummerzheim, D.  
663 (2003). Effect of solar wind pressure pulses on the size and strength of the  
664 auroral oval. *J. Geophys. Res.*, *108*, 8012. doi:10.1029/2002JA009373.
- 665 Brown, R. H., Baines, K. H., Bellucci, G., Bibring, J. P., Buratti, B. J.,  
666 Capaccioni, F., Cerroni, P., Clark, R. N., Coradini, A., Cruikshank, D.,  
667 Drossart, P., Formisano, V., Jaumann, R., Langevin, Y., Matson, D. L.,  
668 McCord, T. B., Mennella, V., Miller, E., Nelson, R. M., Nicholson, P. D.,  
669 Sicardy, B., & Sotin, C. (2004). The Cassini Visual and Infrared Map-  
670 ping Spectrometer (VIMS) investigation. *Space Sci. Rev.*, *115*, 111–168.  
671 doi:10.1007/s11214-004-1453-x.
- 672 Bunce, E. J., Arridge, C. S., Clarke, J. T., Coates, A. J., Cowley, S. W. H.,  
673 Dougherty, M. K., Gérard, J.-C., Grodent, D., Hansen, K. C., Nichols,  
674 J. D., Southwood, D. J., & Talboys, D. L. (2008a). Origin of Saturn's  
675 aurora: Simultaneous observations by Cassini and the Hubble Space Tele-  
676 scope. *J. Geophys. Res.*, *113*. doi:10.1029/2008JA013257.
- 677 Bunce, E. J., Arridge, C. S., Cowley, S. W. H., & Dougherty, M. K. (2008b).  
678 Magnetic field structure of Saturn's dayside magnetosphere and its map-  
679 ping to the ionosphere: Results from ring current modeling. *J. Geo-*  
680 *phys. Res.*, *113*. doi:10.1029/2007JA012538.
- 681 Bunce, E. J., Cowley, S. W. H., & Milan, S. E. (2005a). Interplanetary  
682 magnetic field control of Saturn's polar cusp aurora. *Ann. Geophys.*, *23*,  
683 1405–1431. doi:10.5194/angeo-23-1405-2005.

- 684 Bunce, E. J., Cowley, S. W. H., Talboys, D. L., Dougherty, M. K., Lamy,  
685 L., Kurth, W. S., Schippers, P., Cecconi, B., Zarka, P., Arridge, C. S.,  
686 & Coates, A. J. (2010). Extraordinary field-aligned current signatures  
687 in Saturn's high-latitude magnetosphere: Analysis of Cassini data during  
688 Revolution 89. *J. Geophys. Res.*, *115*, 10238. doi:10.1029/2010JA015612.
- 689 Bunce, E. J., Cowley, S. W. H., Wright, D. M., Coates, A. J., Dougherty,  
690 M. K., Krupp, N., Kurth, W. S., & Rymer, A. M. (2005b). In situ observa-  
691 tions of a solar wind compression-induced hot plasma injection in Saturn's  
692 tail. *Geophys. Res. Lett.*, *322*, L20S04. doi:10.1029/2005GL022888.
- 693 Bunce, E. J., Grodent, D. C., Jinks, S. L., Andrews, D. J., Badman, S. V.,  
694 Cowley, S. W. H., Dougherty, M. K., Kurth, W. S., Mitchell, D. G., Coates,  
695 A. J., & Provan, G. (2014). Cassini nightside observations of the oscillatory  
696 motion of Saturn's northern auroral oval. *J. Geophys. Res.*, *119*, 3528–  
697 3543. doi:10.1002/2013JA019527.
- 698 Burton, M. E., Dougherty, M. K., & Russell, C. T. (2010). Sat-  
699 urn's internal planetary magnetic field. *Geophys. Res. Lett.*, *37*.  
700 doi:10.1029/2010GL045148.
- 701 Carbary, J. F. (2012). The morphology of Saturn's ultraviolet aurora. *J. Geo-*  
702 *phys. Res.*, *117*. doi:10.1029/2012JA017670.
- 703 Carbary, J. F. (2013). Longitude dependences of Saturn's ultraviolet aurora.  
704 *Geophys. Res. Lett.*, *40*, 1902–1906. doi:10.1002/grl.50430.
- 705 Carbary, J. F., & Mitchell, D. G. (2013). Periodicities in Saturn's magneto-  
706 sphere. *Rev. Geophys.*, *51*, 1–30. doi:10.1002/rog.20006.

- 707 Clarke, J. T., Gérard, J.-C., Grodent, D., Wannawichian, S., Gustin, J.,  
708 Connerney, J., Crary, F., Dougherty, M., Kurth, W., Cowley, S. W. H.,  
709 Bunce, E. J., Hill, T., & Kim, J. (2005). Morphological differences between  
710 Saturn's ultraviolet aurorae and those of Earth and Jupiter. *Nature*, *433*,  
711 717–719. doi:10.1038/nature03331.
- 712 Clarke, J. T., Nichols, J., Gerard, J. C., Grodent, D., Hansen, K. C., Kurth,  
713 W., Gladstone, G. R., Duval, J., Wannawichian, S., Bunce, E., Cow-  
714 ley, S. W. H., Crary, F., Dougherty, M., Lamy, L., Mitchell, D., Pryor,  
715 W., Retherford, K., Stallard, T., Zieger, B., Zarka, P., & Cecconi, B.  
716 (2009). Response of Jupiter's and Saturn's auroral activity to the solar  
717 wind. *J. Geophys. Res.*, *114*. doi:10.1029/2008JA013694.
- 718 Cowley, S. W. H., Badman, S. V., Bunce, E. J., Clarke, J. T., Gérard, J.-C.,  
719 Grodent, D., Jackman, C. M., Milan, S. E., & Yeoman, T. K. (2005). Re-  
720 connection in a rotation-dominated magnetosphere and its relation to Sat-  
721 urn's auroral dynamics. *J. Geophys. Res.*, *110*. doi:10.1029/2004JA010796.
- 722 Crary, F., Clarke, J., Dougherty, M., Hanlon, P., Hansen, K., Steinberg, J.,  
723 Barraclough, B., Coates, A., Gerard, J., Grodent, D., Kurth, W., Mitchell,  
724 D., Rymer, A., & Young, D. (2005). Solar wind dynamic pressure and  
725 electric field as the main factors controlling Saturn's aurorae. *Nature*,  
726 *433*, 720–722. doi:DOI 10.1038/nature03333.
- 727 Dougherty, M. K., Achilleos, N., André, N., Arridge, C. S., Balogh, A.,  
728 Bertucci, C., Burton, M. E., Cowley, S. W. H., Erdos, G., Giampieri, G.,  
729 Glassmeier, K. H., Khurana, K. K., Leisner, J., Neubauer, F. M., Russell,  
730 C. T., Smith, E. J., Southwood, D. J., & Tsurutani, B. T. (2005). Cassini



731 magnetometer observations during Saturn orbit insertion. *Science*, 307,  
732 1266–1270. doi:10.1126/science.1106098.

733 Dougherty, M. K., Kellock, S., Southwood, D. J., Balogh, A., Smith, E. J.,  
734 Tsurutani, B. T., Gerlach, B., Glassmeier, K.-H., Gleim, F., Russell,  
735 C. T., Erdos, G., Neubauer, F. M., & Cowley, S. W. H. (2004). The  
736 Cassini Magnetic Field Investigation. *Space Sci. Rev.*, 114, 331–383.  
737 doi:10.1007/s11214-004-1432-2.

738 Esposito, L. W., Barth, C. A., Colwell, J. E., Lawrence, G. M., McClintock,  
739 W. E., Stewart, A. I. F., Keller, H. U., Korth, A., Lauche, H., Festou,  
740 M. C., Lane, A. L., Hansen, C. J., Maki, J. N., West, R. A., Jahn, H.,  
741 Reulke, R., Warlich, K., Shemansky, D. E., & Yung, Y. L. (2004). The  
742 Cassini Ultraviolet Imaging Spectrograph Investigation. *Space Sci. Rev.*,  
743 115, 299–361. doi:10.1007/s11214-004-1455-8.

744 Gérard, J.-C., Bonfond, B., Gustin, J., Grodent, D., Clarke, J. T., Bisikalo,  
745 D., & Shematovich, V. (2009). Altitude of Saturn's aurora and its im-  
746 plications for the characteristic energy of precipitated electrons. *Geo-*  
747 *phys. Res. Lett.*, 36. doi:10.1029/2008GL036554.

748 Gérard, J.-C., Bunce, E. J., Grodent, D., Cowley, S. W. H., Clarke, J. T.,  
749 & Badman, S. V. (2005). Signature of Saturn's auroral cusp: Simultane-  
750 ous Hubble Space Telescope FUV observations and upstream solar wind  
751 monitoring. *J. Geophys. Res.*, 110. doi:10.1029/2005JA011094.

752 Grodent, D., Gérard, J.-C., Cowley, S. W. H., Bunce, E. J., & Clarke,

- 753 J. T. (2005). Variable morphology of Saturn's southern ultraviolet aurora.  
754 *J. Geophys. Res.*, *110*. doi:10.1029/2004JA010983.
- 755 Grodent, D., Gustin, J., Gérard, J.-C., Radioti, A., Bonfond, B., & Pryor,  
756 W. R. (2011). Small-scale structures in Saturn's ultraviolet aurora. *J. Geo-*  
757 *phys. Res.*, *116*. doi:10.1029/2011JA016818.
- 758 Gurnett, D. A., Kurth, W. S., Kirchner, D. L., Hospodarsky, G. B.,  
759 Averkamp, T. F., Zarka, P., Lecacheux, A., Manning, R., Roux, A., Canu,  
760 P., Cornilleau-Wehrin, N., Galopeau, P., Meyer, A., Boström, R., Gustafss-  
761 son, G., Wahlund, J.-E., Åhlen, L., Rucker, H. O., Ladreiter, H. P.,  
762 Macher, W., Woolliscroft, L. J. C., Alleyne, H., Kaiser, M. L., Desch,  
763 M. D., Farrell, W. M., Harvey, C. C., Louarn, P., Kellogg, P. J., Goetz,  
764 K., & Pedersen, A. (2004). The Cassini Radio and Plasma Wave Investi-  
765 gation. *Space Sci. Rev.*, *114*, 395–463. doi:10.1007/s11214-004-1434-0.
- 766 Gurnett, D. A., Persoon, A. M., Kopf, A. J., Kurth, W. S., Morooka, M. W.,  
767 Wahlund, J.-E., Khurana, K. K., Dougherty, M. K., Mitchell, D. G., Krim-  
768 igis, S. M., & Krupp, N. (2010). A plasmopause-like density boundary at  
769 high latitudes in Saturn's magnetosphere. *Geophys. Res. Lett.*, *37*, 16806.  
770 doi:10.1029/2010GL044466.
- 771 Jackman, C. M., Achilleos, N., Bunce, E. J., Cowley, S. W. H., Dougherty,  
772 M. K., Jones, G. H., Milan, S. E., & Smith, E. J. (2004). Interplanetary  
773 magnetic field at  $\sim 9$  AU during the declining phase of the solar cycle and  
774 its implications for Saturn's magnetospheric dynamics. *J. Geophys. Res.*,  
775 *109*. doi:10.1029/2004JA010614.

776 Jackman, C. M., Achilleos, N., Cowley, S. W. H., Bunce, E. J., Radioti, A.,  
777 Grodent, D., Badman, S. V., Dougherty, M. K., & Pryor, W. (2013). Au-  
778 roral counterpart of magnetic field dipolarizations in Saturn's tail. *Planet.*  
779 *Space. Sci.*, *82*, 34–42.

780 Jackman, C. M., Lamy, L., Freeman, M. P., Zarka, P., Cecconi, B., Kurth,  
781 W. S., Cowley, S. W. H., & Dougherty, M. K. (2009). On the char-  
782 acter and distribution of lower-frequency radio emissions at Saturn and  
783 their relationship to substorm-like events. *J. Geophys. Res.*, *114*, 8211.  
784 doi:10.1029/2008JA013997.

785 Jackman, C. M., Slavin, J. A., & Cowley, S. W. H. (2011). Cassini obser-  
786 vations of plasmoid structure and dynamics: Implications for the role of  
787 magnetic reconnection in magnetospheric circulation at Saturn. *J. Geo-*  
788 *phys. Res.*, *116*. doi:10.1029/2011JA016682.

789 Jia, X., Hansen, K. C., Gombosi, T. I., Kivelson, M. G., Tóth, G., DeZeeuw,  
790 D. L., & Ridley, A. J. (2012). Magnetospheric configuration and dynamics  
791 of Saturn's magnetosphere: A global MHD simulation. *J. Geophys. Res.*,  
792 *117*. doi:10.1029/2012JA017575.

793 Kopf, A. J. (2010). *A multi-instrument study of auroral hiss at Saturn*. Ph.D.  
794 thesis University of Iowa.

795 Krimigis, S. M., Mitchell, D. G., Hamilton, D. C., Livi, S., Dandouras, J.,  
796 Jaskulek, S., Armstrong, T. P., Boldt, J. D., Cheng, A. F., Gloeckler, G.,  
797 Hayes, J. R., Hsieh, K. C., Ip, W.-H., Keath, E. P., Kirsch, E., Krupp, N.,  
798 Lanzerotti, L. J., Lundgren, R., Mauk, B. H., McEntire, R. W., Roelof,

- 799 E. C., Schlemm, C. E., Tossman, B. E., Wilken, B., & Williams, D. J.  
800 (2004). Magnetosphere Imaging Instrument (MIMI) on the Cassini Mission  
801 to Saturn/Titan. *Space Sci. Rev.*, *114*, 233–329. doi:10.1007/s11214-004-  
802 1410-8.
- 803 Kurth, W. S., Gurnett, D. A., Clarke, J. T., Zarka, P., Desch, M. D., Kaiser,  
804 M. L., Cecconi, B., Lecacheux, A., Farrell, W. M., Galopeau, P., Gérard,  
805 J.-C., Grodent, D., Prangé, R., Dougherty, M. K., & Crary, F. J. (2005).  
806 An Earth-like correspondence between Saturn’s auroral features and radio  
807 emission. *Nature*, *433*, 722–725. doi:10.1038/nature03334.
- 808 Lamy, L., Cecconi, B., Prangé, R., Zarka, P., Nichols, J. D., & Clarke,  
809 J. T. (2009). An auroral oval at the footprint of Saturn’s kilometric radio  
810 sources, colocated with the UV aurorae. *J. Geophys. Res.*, *114*, A10212.  
811 doi:10.1029/2009JA014401.
- 812 Lamy, L., Prangé, R., Pryor, W., Gustin, J., Badman, S. V., Melin, H.,  
813 Stallard, T., Mitchell, D. G., & Brandt, P. C. (2013). Multi-spectral si-  
814 multaneous diagnosis of Saturn’s aurorae throughout a planetary rotation.  
815 *J. Geophys. Res.*, *118*, 1–27. doi:10.1002/jgra.50404.
- 816 Melin, H., Badman, S. V., Stallard, T. S., Dyudina, U., Nichols, J.,  
817 O’Donoghue, J., Pryor, W. R., Baines, K. H., Miller, S., Gustin, J., Radi-  
818 oti, A., Tao, C., Meredith, C. J., & Blake, J. S. D. (2014). Simultaneous  
819 multi-scale and multi-instrument observations of Saturn’s aurorae during  
820 the 2013 Observing Campaign. *Icarus*, *submitted*.
- 821 Melin, H., Stallard, T., Miller, S., Gustin, J., M., G., Badman, S. V., Pryor,

- 822 W. R., O'Donoghue, J., Brown, R. H., & Baines, K. H. (2011). Simulta-  
823 neous Cassini VIMS and UVIS observations of Saturn's southern aurora:  
824 comparing emissions from H, H<sub>2</sub> and H<sub>3</sub><sup>+</sup> at a high spatial resolution. *Geo-*  
825 *phys. Res. Lett.*, *38*. doi:10.1029/2011GL048457.
- 826 Meredith, C. J., Alexeev, I. I., Badman, S. V., Belenkaya, E. S., Cowley,  
827 S. W. H., Dougherty, M. K., Kalegaev, V. V., Lewis, G. R., & Nichols,  
828 J. D. (2014). Saturn's dayside UV auroras: Evidence for morphological  
829 dependence on the direction of the upstream interplanetary magnetic field.  
830 *J. Geophys. Res.*, *119*. doi:10.1002/2013JA019598.
- 831 Meredith, C. J., Cowley, S. W. H., Hansen, K. C., Nichols, J. D., & Yeoman,  
832 T. K. (2013). Simultaneous conjugate observations of small-scale structures  
833 in Saturn's dayside ultraviolet auroras – implications for physical origins.  
834 *J. Geophys. Res.*, *118*, 2244–2266. doi:10.1002/jgra.50270.
- 835 Mitchell, D. G., Carbary, J. F., Bunce, E. J., Radioti, A., Badman, S. V.,  
836 Pryor, W. R., Hospodarsky, G. B., & Kurth, W. S. (2014). Recurrent  
837 Pulsations in Saturn's High Latitude Magnetosphere. *Icarus*, *submitted*.
- 838 Mitchell, D. G., Krimigis, S. M., Paranicas, C., Brandt, P. C., Carbary, J. F.,  
839 Roelof, E. C., Kurth, W. S., Gurnett, D. A., Clarke, J. T., Nichols, J. D.,  
840 Gérard, J.-C., Grodent, D. C., Dougherty, M. K., & Pryor, W. R. (2009a).  
841 Recurrent energization of plasma in the midnight-to-dawn quadrant of Sat-  
842 urn's magnetosphere, and its relationship to auroral UV and radio emis-  
843 sions. *Planet. Space. Sci.*, *57*, 1732–1742. doi:10.1016/j.pss.2009.04.002.
- 844 Mitchell, D. G., Kurth, W. S., Hospodarsky, G. B., Krupp, N., Saur,

845 J., Mauk, B. H., Carbary, J. F., Krimigis, S. M., Dougherty, M. K.,  
846 & Hamilton, D. C. (2009b). Ion conics and electron beams associ-  
847 ated with auroral processes on Saturn. *J. Geophys. Res.*, *114*, A02212.  
848 doi:10.1029/2008JA013621.

849 Nichols, J. D., Badman, S. V., Baines, K. H., Brown, R. H., Bunce, E. J.,  
850 Clarke, J. T., Cowley, S. W. H., Crary, F. J., Gérard, J.-C., Grocott, A.,  
851 Grodent, D., Kurth, W. S., Melin, H., Mitchell, D. G., Pryor, W. R., &  
852 Stallard, T. S. (2014). Dynamic auroral storms on Saturn as observed  
853 by the Hubble Space Telescope. *Geophys. Res. Lett.*, *41*, 3323–3330.  
854 doi:10.1002/2014GL060186.

855 Nichols, J. D., Cecconi, B., Clarke, J. T., Cowley, S. W. H., Gérard, J.-  
856 C., Grocott, A., Grodent, D., Lamy, L., & Zarka, P. (2010a). Varia-  
857 tion of Saturn’s UV aurora with SKR phase. *Geophys. Res. Lett.*, *37*.  
858 doi:10.1029/2010GL044057.

859 Nichols, J. D., Clarke, J. T., Cowley, S. W. H., Duval, J., Farmer,  
860 A. J., Gérard, J.-C., Grodent, D., & Wannawichian, S. (2008). Os-  
861 cillation of Saturn’s southern auroral oval. *J. Geophys. Res.*, *113*.  
862 doi:10.1029/2008JA013444.

863 Nichols, J. D., Clarke, J. T., Gérard, J. C., Grodent, D., & Hansen, K. C.  
864 (2009). Variation of different components of Jupiter’s auroral emission.  
865 *J. Geophys. Res.*, *114*, 6210. doi:10.1029/2009JA014051.

866 Nichols, J. D., Cowley, S. W. H., & Lamy, L. (2010b). Dawn-dusk oscillation

867 of Saturn's conjugate auroral ovals. *Geophys. Res. Lett.*, *372*, L24102.  
868 doi:10.1029/2010GL045818.

869 Prangé, R., Pallier, L., Hansen, K. C., Howard, R., Vourlidas, A., Courtin,  
870 R., & Parkinson, C. (2004). An interplanetary shock traced by plan-  
871 etary auroral storms from the Sun to Saturn. *Nature*, *432*, 78–81.  
872 doi:10.1038/nature02986.

873 Provan, G., Andrews, D. J., Arridge, C. S., Coates, A. J., Cowley, S. W. H.,  
874 Milan, S. E., Dougherty, M. K., & Wright, D. M. (2009). Polariza-  
875 tion and phase of planetary-period magnetic field oscillations on high-  
876 latitude field lines in Saturn's magnetosphere. *J. Geophys. Res.*, *114*,  
877 2225. doi:10.1029/2008JA013782.

878 Provan, G., Lamy, L., Cowley, S. W. H., & Dougherty, M. K. (2014).  
879 Planetary period oscillations in Saturn's magnetosphere: Comparison of  
880 magnetic oscillations and SKR modulations in the post-equinox interval.  
881 *J. Geophys. Res.*, *in press*. doi:10.1002/2014JA020011.

882 Radioti, A., Grodent, D., Gérard, J.-C., Bonfond, B., Gustin, J., Pryor, W.,  
883 Jasinski, J. M., & Arridge, C. S. (2013a). Auroral signatures of multiple  
884 magnetopause reconnection at Saturn. *Geophys. Res. Lett.*, *40*, 4498–4502.  
885 doi:10.1002/grl.50889.

886 Radioti, A., Grodent, D., Gérard, J.-C., Bonfond, B., Pryor, W., Gustin, J.,  
887 Mitchell, D., & Jackman, C. M. (2014). A remarkable magnetotail recon-  
888 nection event at Saturn as observed by UVIS/Cassini. *Icarus*, *submitted*.

- 889 Radioti, A., Grodent, D., Gérard, J.-C., Milan, S. E., Bonfond, B., Gustin, J.,  
890 & Pryor, W. R. (2011). Bifurcations of the main auroral ring at Saturn:  
891 ionospheric signatures of consecutive reconnection events at the magne-  
892 topause. *J. Geophys. Res.*, *116*. doi:10.1029/2011JA016661.
- 893 Radioti, A., Roussos, E., Grodent, D., Gérard, J.-C., Krupp, N., Mitchell,  
894 D. G., Gustin, J., Bonfond, B., & Pryor, W. (2013b). Signatures of magne-  
895 topheric injections in Saturn's aurora. *J. Geophys. Res.*, *118*, 1922–1933.  
896 doi:10.1002/jgra.50161.
- 897 Roussos, E., Krupp, N., Mitchell, D. G., Paranicas, C., Krimigis, S. M., An-  
898 driopoulou, M., Kurth, W. S., Masters, A., & Dougherty, M. K. (2014).  
899 Quasi-periodic injections of relativistic electrons in Saturn's outer magne-  
900 tosphere. *Icarus*, *submitted*.
- 901 Sandel, B. R., Shemansky, D. E., Broadfoot, A. L., Holberg, J. B., Smith,  
902 G. R., McConnell, J. C., Strobel, D. F., Atreya, S. K., Donahue, T. M.,  
903 Moos, H. W., Hunten, D. M., Pomphrey, R. B., & Linick, S. (1982). Ex-  
904 treme ultraviolet observations from the Voyager 2 encounter with Saturn.  
905 *Science*, *215*, 548–553. doi:10.1126/science.215.4532.548.
- 906 Stallard, T. S., Melin, H., Miller, S., Badman, S. V., Brown, R. H., &  
907 Baines, K. H. (2012). Peak emission altitude of Saturn's  $H_3^+$  aurora. *Geo-*  
908 *phys. Res. Lett.*, *39*. doi:10.1029/2012GL052806.
- 909 Talboys, D. L., Arridge, C. S., Bunce, E. J., Coates, A. J., Cowley, S. W. H.,  
910 & Dougherty, M. K. (2009a). Characterization of auroral current systems



- 911 in Saturn's magnetosphere: High-latitude Cassini observations. *J. Geo-*  
912 *phys. Res.*, *114*. doi:10.1029/2008JA013846.
- 913 Talboys, D. L., Arridge, C. S., Bunce, E. J., Coates, A. J., Cowley, S. W. H.,  
914 Dougherty, M. K., & Khurana, K. K. (2009b). Signatures of field-aligned  
915 currents in Saturn's nightside magnetosphere. *Geophys. Res. Lett.*, *36*.  
916 doi:10.1029/2009GL039867.
- 917 Talboys, D. L., Bunce, E. J., Cowley, S. W. H., Arridge, C. S., Coates,  
918 A. J., & Dougherty, M. K. (2011). Statistical characteristics of field-  
919 aligned currents in Saturn's nightside magnetosphere. *J. Geophys. Res.*,  
920 *116*. doi:10.1029/2010JA016102.
- 921 Tao, C., Badman, S. V., & Fujimoto, M. (2011). UV and IR auroral emission  
922 model for the outer planets: Jupiter and Saturn comparison. *Icarus*, *213*,  
923 581–592. doi:10.1016/j.icarus.2011.04.001.
- 924 Thomsen, M. F. (2013). Saturn's magnetospheric dynamics. *Geo-*  
925 *phys. Res. Lett.*, *40*, 5337–5344. doi:10.1002/2013GL057967.

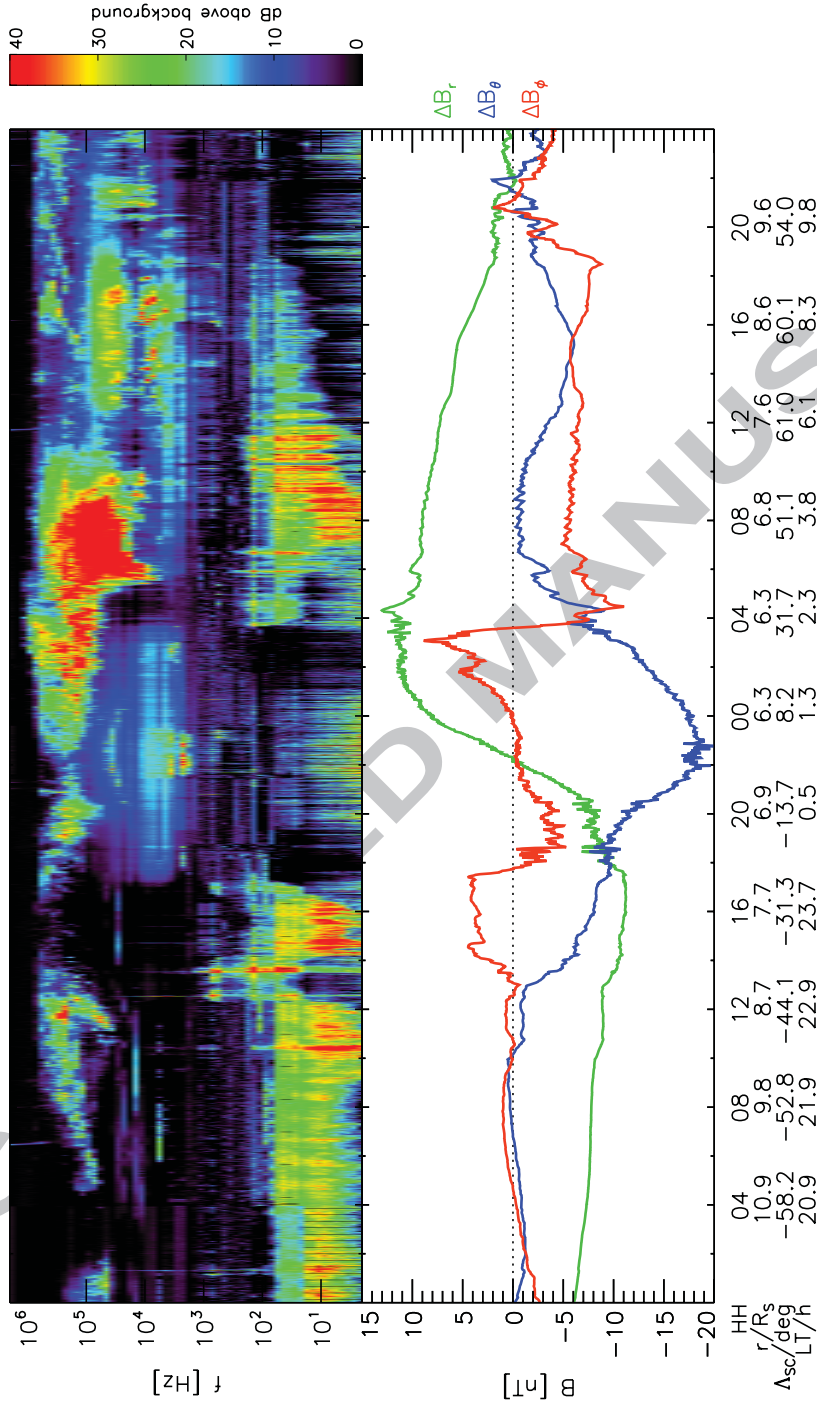


Figure 1: Field and plasma measurements made by Cassini during 2013-111 and 2013-112 (21 and 22 April). The top panel shows the wave frequency-time spectrogram measured by Cassini/RPWS. The bottom panel shows the residual components of the magnetic field in spherical polar coordinates. Cassini ephemeris data are also labelled on the x-axis, where  $r$  is the radial distance of the spacecraft from Saturn's centre,  $\Lambda_{SC}$  is the sub-spacecraft latitude, and LT is the local time.

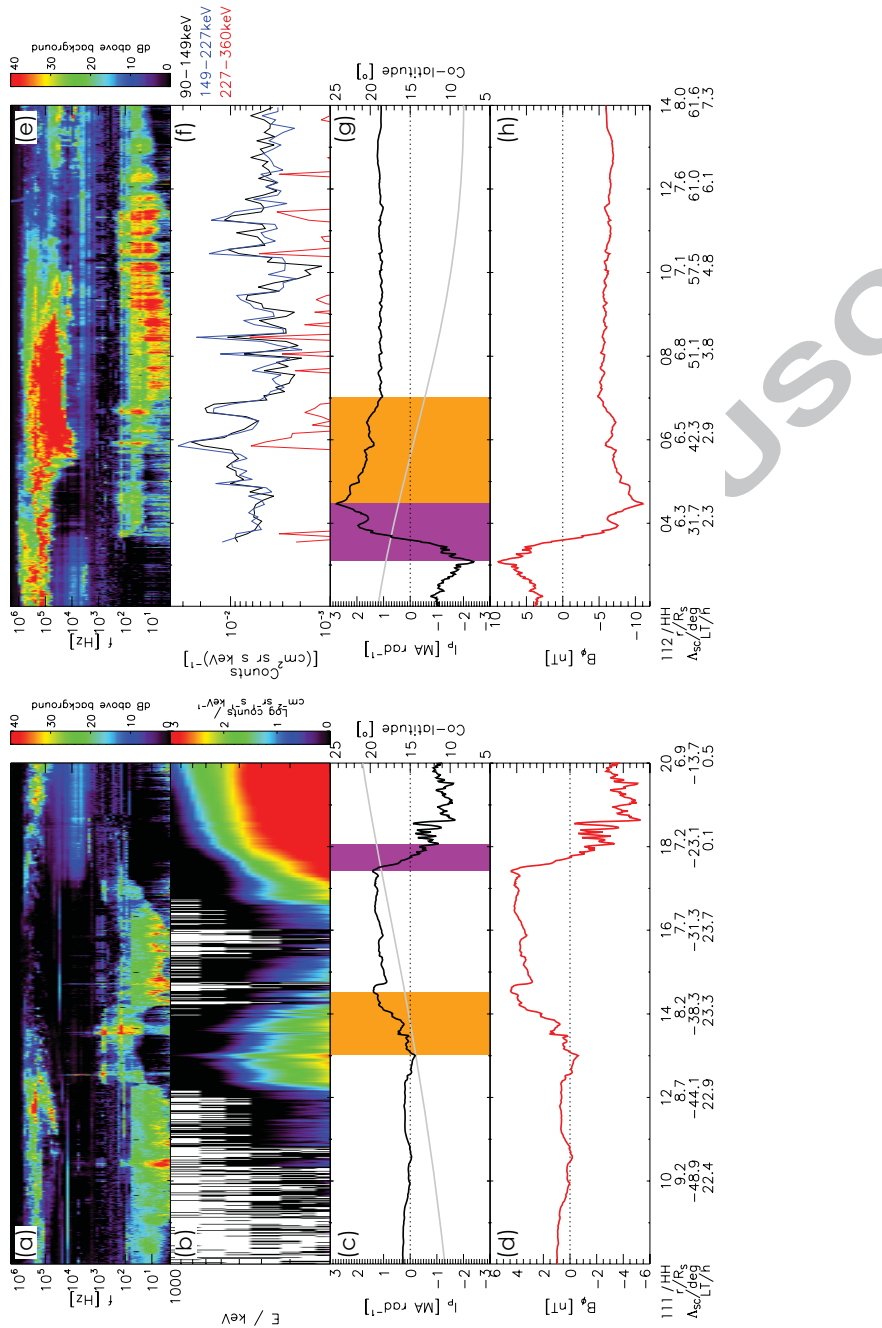


Figure 2: Auroral field-aligned currents measured by Cassini on 2013-111 08-20 UT and 2013-112 02-14 UT. (a) and (e) frequency-time spectrograms of waves measured by Cassini/RPWS. (b) fluxes of 200 keV–1 MeV electrons detected by LEMMS. (c) and (g) ionospheric colatitude of the spacecraft using a magnetic field model to map along the field line (grey line, right hand axis), and the meridional ionospheric Pedersen current per radian, positive equatorward (black line, left hand axis). (d) and (h)  $B_\phi$  component of the magnetic field. (f) energetic proton counts at 90–360 keV detected by INCA.

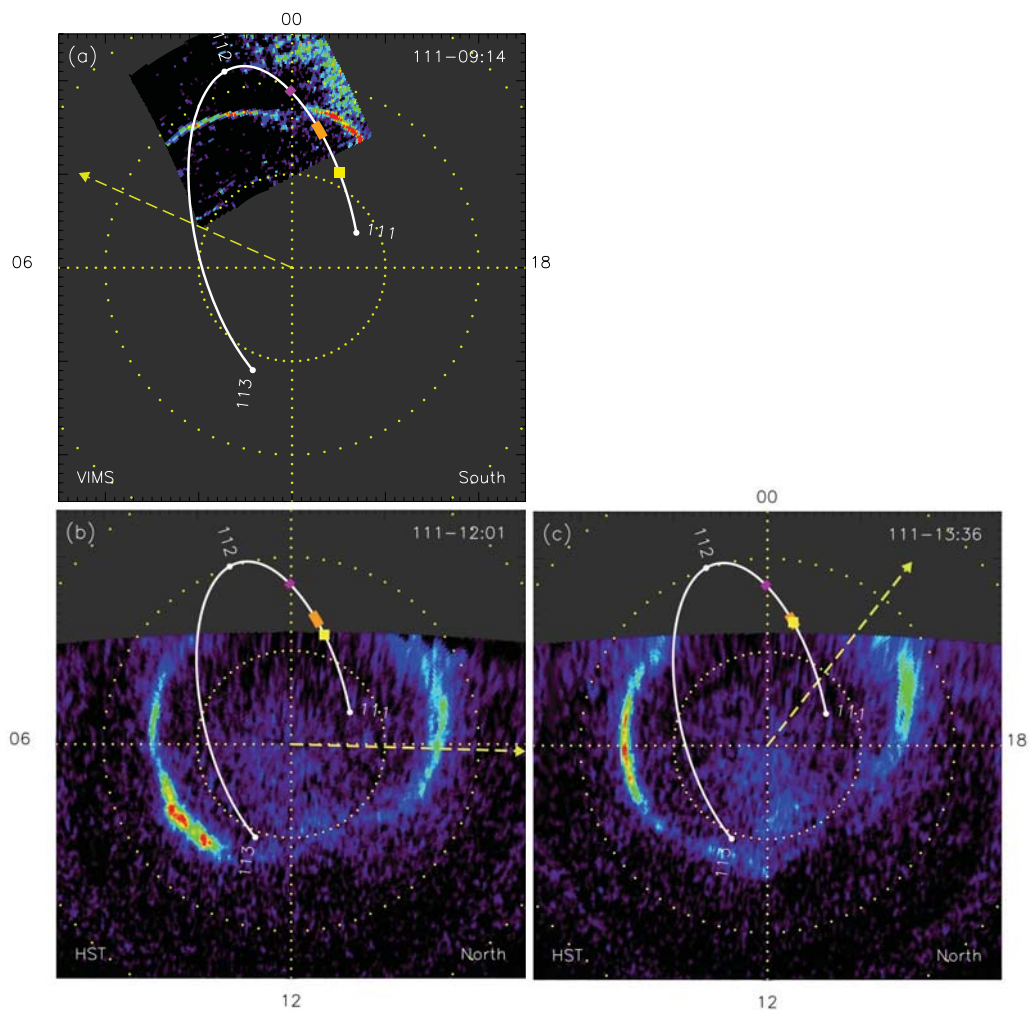


Figure 3: Observations of Saturn's aurorae on 2013-111. Local noon is to the bottom and dawn to the left. The yellow grid marks circles of latitude at intervals of  $10^\circ$  and the noon-midnight and dawn-dusk meridians. The white line shows the ionospheric footprint of Cassini's trajectory on 2013-111 to 2013-113 mapped into the appropriate ionosphere. The yellow square on this line indicates the position of Cassini at the time this image was taken, while the purple and orange shaded regions show the location of the upward and downward field-aligned current regions, respectively, determined from the magnetic field data in this hemisphere. The yellow dashed arrow indicates the direction in which the auroral oval is expected to be tilted at the time of the image. The hemisphere imaged and instrument used are labelled in the bottom of each panel.

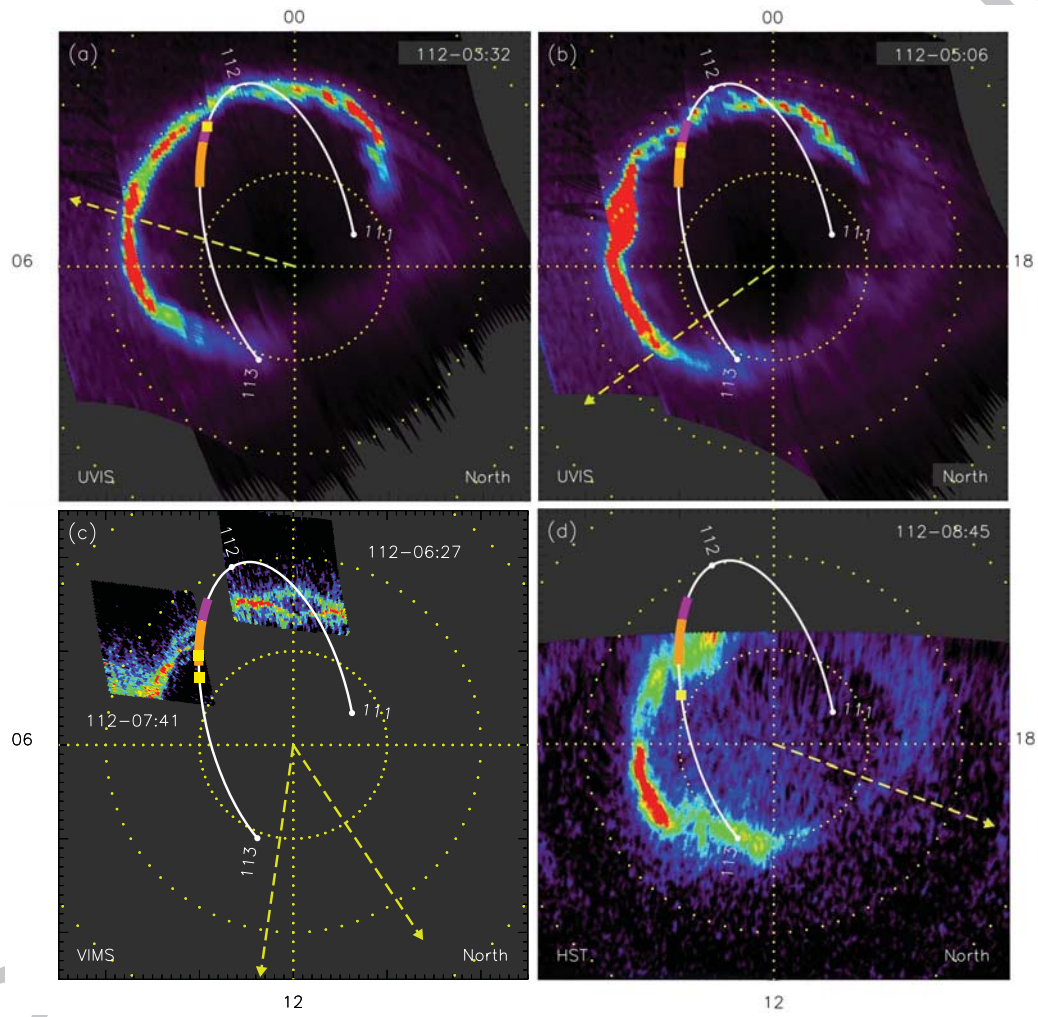


Figure 4: Observations of Saturn's aurorae on 2013-112 in the same format as Figure 3.

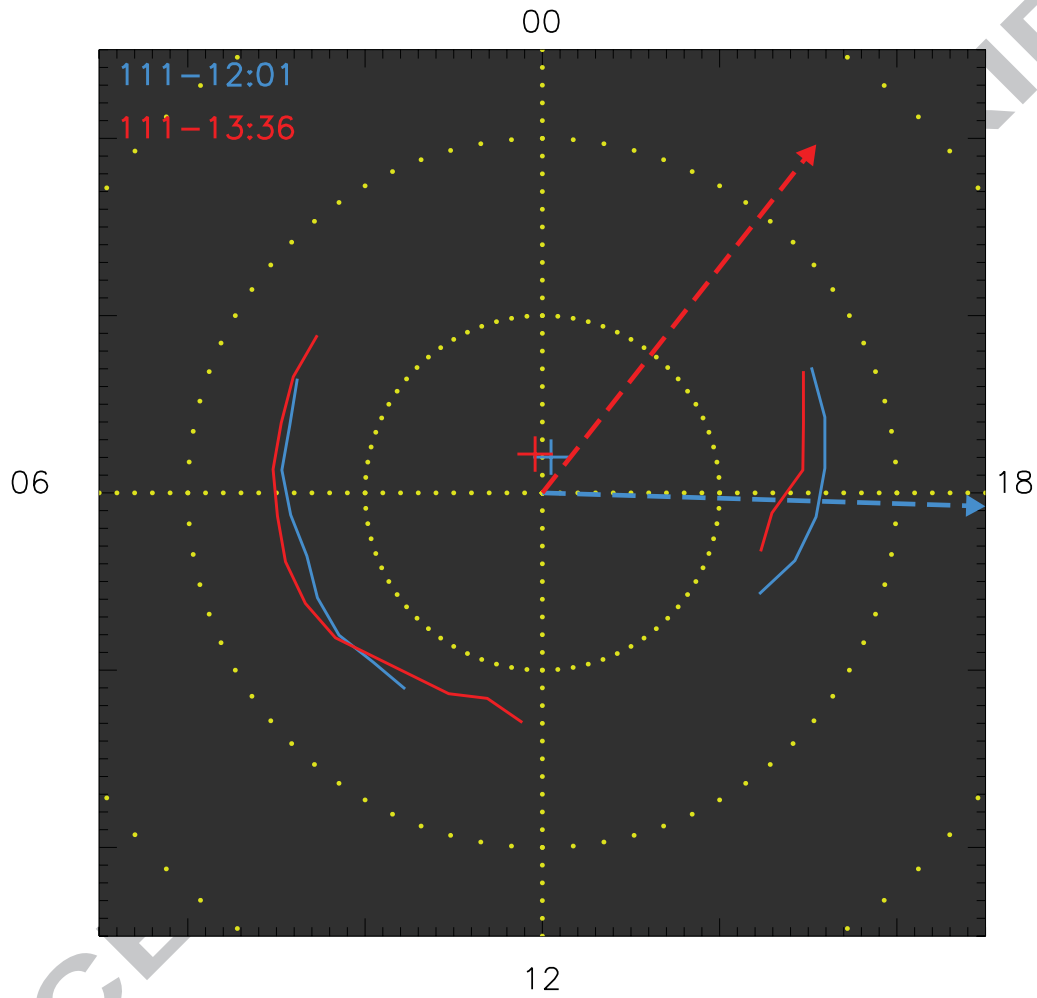


Figure 5: Location of the peak northern auroral emission on 2013-111 in the same orientation as Figure 3. The crosses indicate the centre of a best fit circle in each case. The dashed arrow indicates the direction in which the northern auroral oval is expected to be tilted at the centre time of each image.

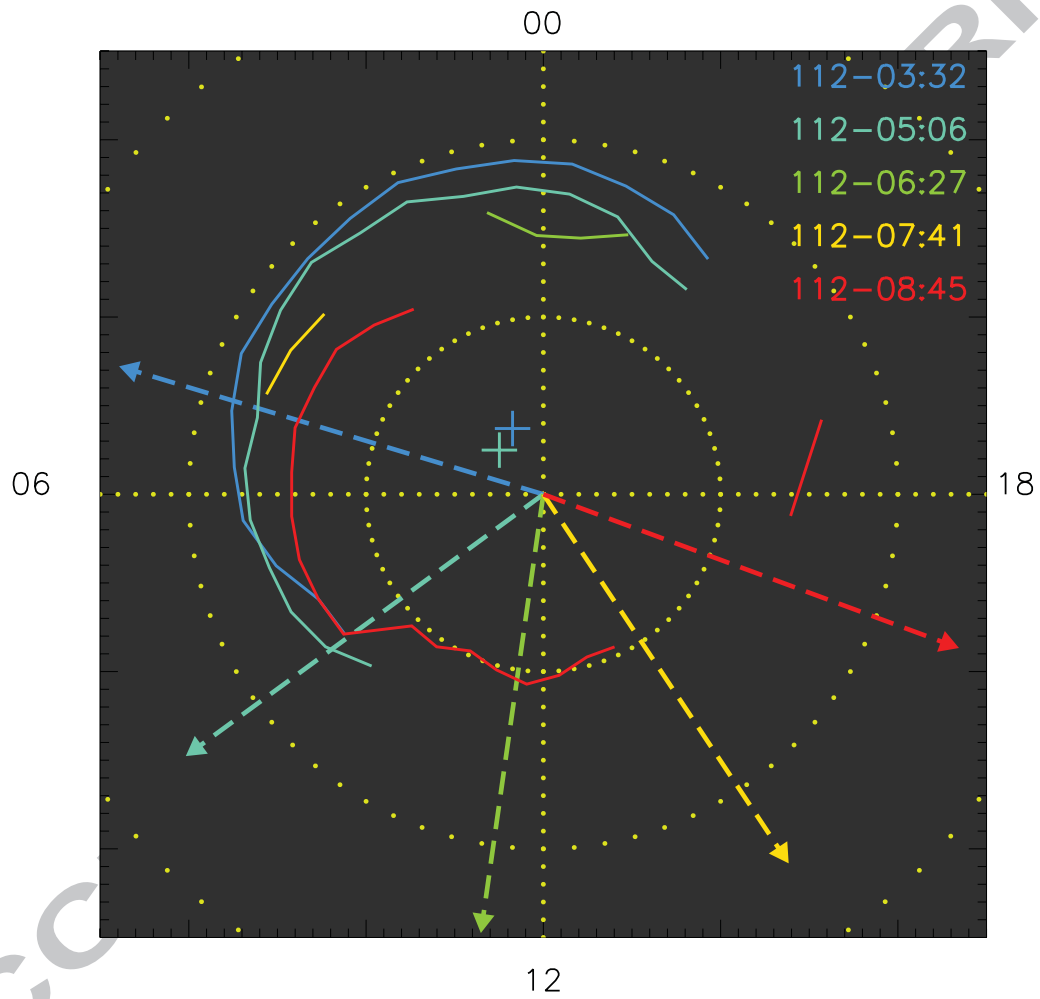


Figure 6: As Figure 5 but for auroral observations on 2013-112.

## Highlights

Saturn's auroral response to a solar wind compression was observed

Nightside auroral field-aligned currents became twice as strong

The nightside auroral arc broadened and moved poleward

This motion is opposite to the expected motion of the oscillating auroral oval